The Astronomical Journal, 154:186 (16pp), 2017 November https://doi.org/10.3847/1538-3881/aa8df6

Resolving the Circumstellar Environment of the Galactic B[e] Supergiant Star MWC 137 from Large to Small Scales*

Michaela Kraus[1,2], Tiina Liimets[2,3], Cristina E. Cappa[4,5], Lydia S. Cidale[5,6,7], Dieter H. Nickeler[1], Nicolas U. Duronea[4], Maria L. Arias[5,6], Diah S. Gunawan[7], Mary E. Oksala[8,9], Marcelo Borges Fernandes[10], Grigoris Maravelias[7], Michel Curé[7], and Miguel Santander-García[11]
[1] Astronomický ústav, Akademie věd České republiky, v.v.i., Fričova 298, 251 65 Ondřejov, Czech Republic; michaela.kraus@asu.cas.cz
[2] Tartu Observatory, 61602 Tõravere, Tartumaa, Estonia
[3] Institute of Physics, University of Tartu, Ravila 14c, 50411, Tartu, Estonia
[4] Instituto Argentino de Radioastronomía, CONICET, CCT-La Plata, C.C.5., 1894, Villa Elisa, Argentina
[5] Facultad de Ciencias Astronómicas y Geofísicas, Universidad Nacional de La Plata, Paseo del Bosque s/n, 1900, La Plata, Argentina
[6] Instituto de Astrofísica de La Plata, CCT La Plata, CONICET-UNLP, Paseo del Bosque s/n, 1900, La Plata, Argentina
[7] Instituto de Física y Astronomía, Facultad de Ciencias, Universidad de Valparaíso, Av. Gran Bretaña 1111, Casilla 5030, Valparaíso, Chile
[8] California Lutheran University, Department of Physics, Thousand Oaks, CA 91360, USA
[9] LESIA, Observatoire de Paris, PSL Research University, CNRS, Sorbonne Universités, UPMC Univ. Paris 06, Univ. Paris Diderot, Sorbonne Paris Cité, 5 place Jules Janssen, F-92195 Meudon, France
[10] Observatório Nacional, Rua General José Cristino 77, 20921-400 São Cristovão, Rio de Janeiro, Brazil
[11] Observatorio Astronómico Nacional (IGN), C/Alfonso XII 3, E-28014, Madrid, Spain
Received 2017 August 28; revised 2017 September 18; accepted 2017 September 18; published 2017 October 20

Abstract

The Galactic object MWC 137 has been suggested to belong to the group of B[e] supergiants. However, with its large-scale optical bipolar ring nebula and high-velocity jet and knots, it is a rather atypical representative of this class. We performed multiwavelength observations spreading from the optical to the radio regimes. Based on optical imaging and long-slit spectroscopic data, we found that the northern parts of the large-scale nebula are predominantly blueshifted, while the southern regions appear mostly redshifted. We developed a geometrical model consisting of two double cones. Although various observational features can be approximated with such a scenario, the observed velocity pattern is more complex. Using near-infrared integral-field unit spectroscopy, we studied the hot molecular gas in the vicinity of the star. The emission from the hot CO gas arises in a small-scale disk revolving around the star on Keplerian orbits. Although the disk itself cannot be spatially resolved, its emission is reflected by the dust arranged in arc-like structures and the clumps surrounding MWC 137 on small scales. In the radio regime, we mapped the cold molecular gas in the outskirts of the optical nebula. We found that large amounts of cool molecular gas and warm dust embrace the optical nebula in the east, south, and west. No cold gas or dust was detected in the north and northwestern regions. Despite the new insights into the nebula kinematics gained from our studies, the real formation scenario of the large-scale nebula remains an open issue.

Key words: circumstellar matter – stars: early-type – stars: individual (MWC 137) – stars: massive – supergiants

Supporting material: machine-readable table

1. Introduction

The enigmatic object MWC 137 (V1308 Ori) belongs to the group of Galactic B[e] stars. It is surrounded by the optical nebula Sh 2-266 and located in the center of a cluster. The evolutionary state of MWC 137 has long been debated. Suggestions ranged from pre-main sequence (Berrilli et al. 1992; Hillenbrand et al. 1992; The et al. 1994; Hein Bertelsen et al. 2016) to post-main sequence, spreading over a large luminosity range (Herbig & Kameswara Rao 1972; Finkenzeller & Mundt 1984; Esteban & Fernandez 1998; Oksala et al. 2013).

Significant progress in the star's classification was achieved by Muratore et al. (2015), who modeled the emission from the hot ^{13}CO gas in the vicinity of MWC 137 that was first detected by Oksala et al. (2013). The presence of measurable amounts of ^{13}CO implies a significant enrichment of the circumstellar material in ^{13}C (Kraus 2009). As stellar evolution models show (e.g., Ekström et al. 2012), this isotope is processed inside the star and via mixing processes transported to the surface, from which it is liberated into the environment by mass-loss events. With the discovery of hot, circumstellar ^{13}CO emission, a pre-main sequence evolutionary phase of MWC 137 could finally be excluded.

The evolved nature of MWC 137 is further consolidated by the studies of Mehner et al. (2016). These authors investigated the whole cluster and determined a cluster age of >3 Myr. With a mass of 10–15 $M_\odot$ for MWC 137, this object has clearly evolved off the main sequence.

Moreover, Mehner et al. (2016) discovered a jet with several individual knots emanating from MWC 137 with high velocities.

* Based on observations collected with (1) the ESO VLT Paranal Observatory under programs 094.D-0637(B) and 097.D-0033(A), (2) the MPG 2.2 m telescope at La Silla Observatory, Chile, under programs 096.A-9030(A) and 096.A-9039(A), (3) the Gemini Observatory, which is operated by the Association of Universities for Research in Astronomy, Inc., under a cooperative agreement with the NSF on behalf of the Gemini partnership: the National Science Foundation (United States), the Science and Technology Facilities Council (United Kingdom), the National Research Council (Canada), CONICYT (Chile), the Australian Research Council (Australia), Ministério da Ciência, Tecnologia e Inovação (Brazil), and Ministerio de Ciencia, Tecnología e Innovación Productiva (Argentina), under program GN-2013B-Q-11, (4) the Nordic Optical Telescope, operated by the Nordic Optical Telescope Scientific Association at the Observatorio del Roque de los Muchachos, La Palma, Spain, of the Instituto de Astrofisica de Canarias, (5) the APEX telescope under the program CHILE-9711B-2016. APEX is a collaboration between the Max-Planck-Institut für Radioastronomie, the European Southern Observatory, and the Onsala Observatory, and (6) the Perek 2 m telescope at Ondřejov Observatory, Czech Republic.

Estimates of the age of these knots revealed that the jet must be much younger than the large-scale optical nebula. The position angle of the jet is aligned with the polarization angle and hence perpendicular to the circumstellar disk traced on small scales by intrinsic polarization in Hα (Oudmaijer & Drew 1999). Further confirmation for a rotating circumstellar disk was provided by the rotationally broadened CO bandhead emission reported by Muratore et al. (2015).

The large-scale structure seen in Hα images (e.g., Marston & McCollum 2008) led Esteban & Fernandez (1998) to suggest that Sh 2-266 could be a ring nebula produced by the interaction of the stellar wind with the interstellar medium. On the other hand, as the morphology of Sh 2-266 is reminiscent of the bipolar ring nebulae detected around two early B-type supergiants, Sher 25 (Brandner et al. 1997) and SBW1 (Smith et al. 2007), Muratore et al. (2015) proposed that the nebula material might have been ejected during the blue supergiant phase so that MWC 137 might be transiting from a B[e] supergiant into a blue supergiant with a bipolar ring nebula.

We carried out an observational campaign combining data from various wavelength regimes (optical, infrared, and radio) and on different spatial scales. These data are aimed to investigate in detail the structure and kinematics of the environment of MWC 137 on both large and small scales.

2. Observations and Data Reduction

2.1. Optical Imaging and Spectroscopy

Long-slit optical spectra and imaging data were obtained on 2016 November 8 with the Nordic Optical Telescope (NOT) using the Andalucia Faint Object Spectrograph and Camera (ALFOSC). For the imaging, one long (600 s) and one short (10 s) exposure were obtained using the broadband Hα filter (Halp_658_18 No. 22), which also includes the [N II] $\lambda\lambda$6548,6583 doublet. The short exposure was used to fix the exact stellar coordinates, while the long exposure resolved the spatial structure of the nebula and served as a template to position the slits. ALFOSC's field of view (FOV) is $6\farcm4 \times 6\farcm4$, and the pixel scale is $0\farcs21$ pix^{-1}.

For the long-slit observations, we utilized Grism #17 with a slit width of $0\farcs5$, providing spectral coverage from 6315 to 6760 Å and a spectral reciprocal dispersion of 0.29 Å pix^{-1}. This spectral range was chosen to trace Hα and the strongest nebular lines: [N II] $\lambda\lambda$6548, 6583 and [S II] $\lambda\lambda$6716, 6731. Due to poor weather conditions, only three slit positions could be observed. Two of them were centered on the star and had position angles (PAs) of 35° and 298° (see details in Section 3.2 and Figure 4). For both, an integration time of 30 minutes was used in a single exposure. The third position was chosen slightly off the central star with two field stars as reference points and with a PA of 341°.1. It was aligned such that individual knots, in particular knot c of the jet, were covered. For this position, two exposures of 30 minutes each were acquired and co-added.

The star was also observed with medium resolution using the Coudé spectrograph (Šlechta & Škoda 2002) attached to the Perek 2 m telescope at Ondřejov Observatory. Three spectra were collected, two in the Hα region (6250–6760 Å) on 2011 October 1 and 2013 October 5, and one in the red region (6990–7500 Å) on 2013 October 5. The observations were carried out with the 830.77 lines mm^{-1} grating and a SITe 2030 × 800 CCD for the spectra taken before 2013 June, and a PyLoN 2048 × 512BX CCD for those taken thereafter. With a slit width set at $0\farcs6$, the spectral resolution is $R \simeq 13{,}000$ in the Hα region and $R \simeq 15{,}000$ in the red region.

In addition, we acquired high-resolution spectra on 2015 December 5 and 2016 February 28 with the Fiber-fed Extended Range Optical Spectrograph (FEROS; Kaufer et al. 1999) attached to the MPG 2.2 m telescope at the European Southern Observatory in La Silla (Chile). FEROS is a bench-mounted echelle spectrograph with fibers, which cover a sky area of $2''$ of diameter. The wavelength coverage ranges from 3600 to 9200 Å, and the spectral resolution is $R = 48{,}000$ (in the region around 6000 Å).

To perform telluric corrections, spectra of a standard star, typically a rapidly rotating early-type star, were taken during the observing nights.

The data collected at NOT and Ondřejov were reduced (bias, flat fielding, wavelength calibration) using standard IRAF[12] routines, whereas for the FEROS data, the reduction pipeline was utilized. Telluric correction was performed for the FEROS and the Ondřejov data, and all spectra were corrected for heliocentric velocity.

2.2. Near-infrared Spectroscopy

MWC 137 was observed on 2014 December 30 and 2016 March 19 with the Spectrograph for INtegral Field Observation in the Near-Infrared (SINFONI; Eisenhauer et al. 2003; Bonnet et al. 2004) on the ESO VLT UT4 8 m telescope. The observations were carried out using the $0\farcs8 \times 0\farcs8$ FOV (25 mas plate scale) with the *K*-band grating, which provides a spectral resolution of $R = 4500$ and a wavelength coverage of 1.95–2.45 μm. For proper sky subtraction, the observations were carried out in an ABBA nod pattern with the B position taken $1'$ west of the central star. Data reduction was performed with the ESO SINFONI pipeline (version 2.7.0). Raw frames were corrected for bad pixels, flat fields, and nonlinearity, and were wavelength calibrated.

In addition, the star was observed on 2013 December 14 with the Gemini Near-Infrared Spectrograph (GNIRS) mounted on the Gemini North telescope in the *L*-band. We used the long camera with the 110.5 lines mm^{-1} grating and $0\farcs10$ slit, which we centered on Brα. The achieved spectral resolution is $R \simeq 19{,}000$ with a wavelength coverage of ~0.1 μm. To facilitate sky subtraction, the observations were carried out in an ABBA nod pattern along the slit with an offset of $6''$ between the A and B positions. The data were reduced using standard IRAF routines.

In both cases, a telluric standard star was observed at similar airmass. Telluric and heliocentric velocity corrections of the infrared spectra were performed with standard IRAF tasks.

2.3. Radio Data

Radio observations were taken on 2016 March 21 and 22, July 30 and 31, and August 1 with the Atacama Pathfinder EXperiment (APEX; Güsten et al. 2006) located at Llano de Chajnantor (Chilean Andes). As front end for the observations, we used the APEX-2 receiver ($T_{sys} = 300$ K) of the Swedish Heterodyne Facility Instrument (SHeFI; Vassilev et al. 2008) to

[12] IRAF is distributed by the National Optical Astronomy Observatory, which is operated by the Association of Universities for Research in Astronomy (AURA) under cooperative agreement with the National Science Foundation.

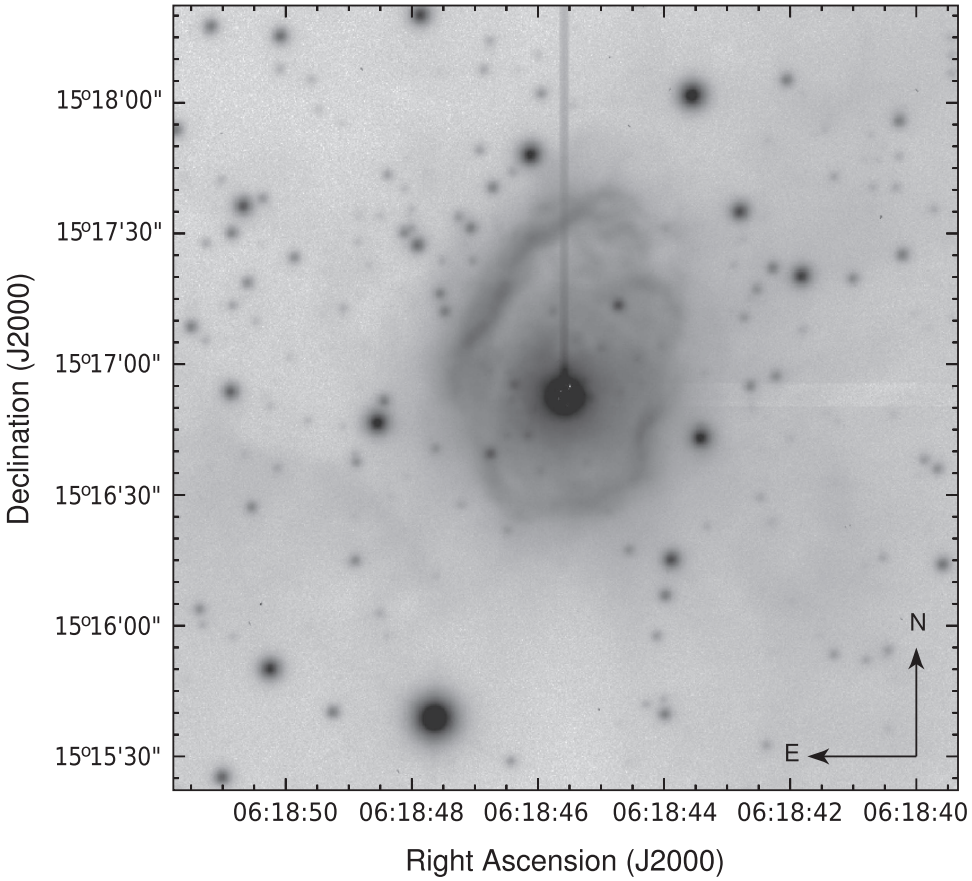

Figure 1. ALFOSC Hα image of the nebula structure around MWC 137. The FOV is $3' \times 3'$. The dark line from the star to the north and the bright wide band to the west are instrumental artifacts.

perform observations of the molecular line ^{12}CO(3–2) at 345.79599 GHz and ^{13}CO(3–2) at 330.58796 GHz, and the APEX-1 receiver (150 K) to observe the SiO(5–4) and CS(5–4) molecular lines at 217.104980 and 244.935644 GHz, respectively. The observations were carried out within an area of $3' \times 3'$ centered at the position of the B[e] star (R.A., Decl. (J2000) = $06^h18^m46^s$, $15°16'50''$).

Observations were made using the on-the-fly (OTF) mode with two orthogonal scan directions along R.A. and Decl. and a space between dumps in the scanning direction of $9''$. Calibration and pointing were performed using IRC +10216, RAFGL 865, OMC1, IK-TAU, R Dor, o Ceti, and CRL 618. The intensity calibration has an uncertainty of 10%.

The backend for the observations was the FFT spectrometer consisting of 4096 channels, with a total bandwidth of 1000 km s^{-1} and a velocity resolution of 0.2 km s^{-1}. Atmospheric attenuation correction was done by skydips, and the output intensity scale given by the system is T_A. The observed intensities were converted to the main-beam brightness temperature scale using $T_{mb} = T_A/\eta_{mb}$, where η_{mb} is the main-beam efficiency. For the SHeFI/APEX-1 and SHeFI/APEX-2 receivers, the adopted value is $\eta_{mb} = 0.73$ (Vassilev et al. 2008). The half-power beam width of the telescope is $\sim 21''$ for the CO lines and $30''$ for the SiO and CS lines. The off-source position free of CO emission was located at R.A., Decl. (J2000) = $6^h34^m33\overset{s}{.}8$, $+16°52'48\overset{''}{.}9$.

The spectra were reduced using the Continuum and Line Analysis Single-dish Software (CLASS90) program of the IRAM GILDAS software package.[13] A linear baseline fitting was applied to the data. The rms noise of the profiles after baseline subtraction and calibration is ~0.3 K for ^{12}CO(3–2) and 0.2 K for ^{13}CO(3–2) per spectral channel. The Astronomical Image Processing System package was used to perform the analysis.

2.4. Complementary Data

We searched for additional information provided in different archives and retrieved images in the infrared and radio continuum from public surveys that complement our own data sets.

The region around MWC 137 was observed in the near- and mid-infrared with the *Wide-field Infrared Survey Explorer* (*WISE*; Wright et al. 2010) satellite. The four bands are centered on 3.4, 4.6, 12.0, and 22.0 μm and have angular resolutions of $6\overset{''}{.}1$, $6\overset{''}{.}4$, $6\overset{''}{.}5$, and $12\overset{''}{.}0$, respectively. Moreover, the Galactic Legacy Infrared Mid-Plane Survey Extraordinaire (GLIMPSE; Churchwell & GLIMPSE Team 2001; Benjamin et al. 2003) imaged MWC 137 using the two Infrared Array Camera (IRAC; Fazio et al. 2004) bandpasses at 3.6 and 4.5 μm on the *Spitzer Space Telescope* (Werner et al. 2004). The angular resolutions are less than $2''$ in all bands.

In the far-infrared (FIR) regime, the *Herschel Space Observatory*[14] imaged MWC 137 at 70 and 160 μm with the

[13] http://www.iram.fr/IRAMFR/GILDAS

[14] *Herschel* is an ESA space observatory with science instruments provided by European-led Principal Investigator consortia and with important participation from NASA (http://www.cosmos.esa.int/web/herschel/science-archive).

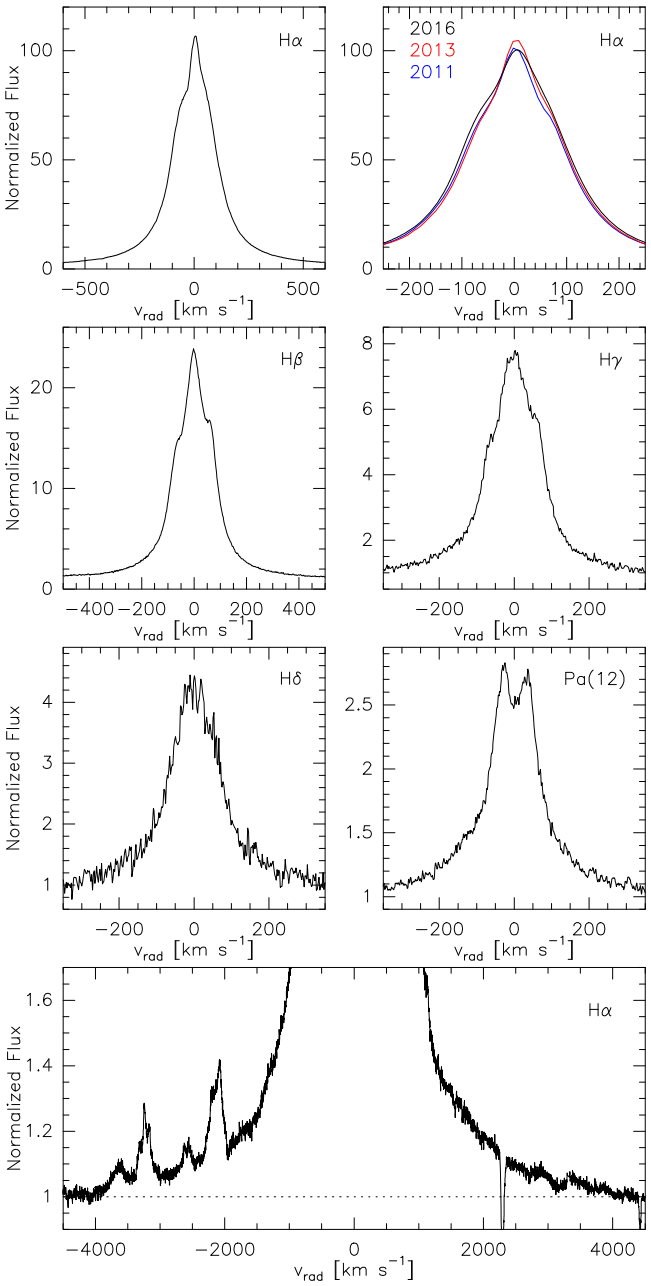

Figure 2. Profiles of the hydrogen lines of the lower Balmer series and of Pa(12). The top-right panel shows the Hα line obtained in Ondřejov in 2011 (blue) and 2013 (red) compared to the profile in the FEROS spectrum from 2016. The latter was convolved to the same low resolution. The broad emission wings of Hα are depicted in the bottom panel.

Photodetector Array Camera and Spectrometer (PACS; Poglitsch et al. 2010) and at 250, 350, and 500 μm with the Spectral and Photometric Imaging REceiver (SPIRE; Griffin et al. 2010). These data were acquired during the *Herschel* Infrared GALactic plane survey (Hi-GAL; Molinari et al. 2010) key program. The angular resolutions at 70, 160, 250, 350, and 500 μm are 8.″5, 13.″5, 18″, 25″, and 36″, respectively.

All infrared images were obtained from the Infrared Science Archive[15] provided by the NASA Infrared Processing and Analysis Center (IPAC). The retrieved *Herschel* images were processed at level 2.5 (PACS) and 3 (SPIRE).

In addition, we retrieved radio continuum data at 1420 MHz that were taken during the NRAO Very Large Array Sky Survey (NVSS; Condon et al. 1998). The images have a spatial resolution of 45″ and an rms noise of about 0.45 mJy beam^{-1} (Stokes *I*).

3. Results

3.1. Star and Optical Nebula

The structure of the optical nebula around MWC 137 is resolved in the long-exposure ALFOSC narrowband image in the Hα+[N II] filter (Figure 1). The nebula has an oval shape with arc-like structures along its outer boundary and a size of 80″ × 60″, similar to what was resolved in earlier observations (Marston & McCollum 2008; Mehner et al. 2016). The ionized nebula displays an asymmetry with respect to the stellar position. It is more extended to the north. We also note diffuse emission at larger distances, in particular to the southeast and southwest of the main nebula.

The Ondřejov and FEROS spectra cover the innermost 0.″6 and 2″, respectively, which contain the star and its closest environment. The spectra does not display obvious photospheric absorption lines, but does display numerous emission lines from both permitted and forbidden transitions of elements in different ionization stages, as was also reported in earlier works of Zickgraf (2003) and Hernández et al. (2004). Absorption features in the spectra are due to diffuse interstellar bands and cool material in foreground clouds traceable, e.g., via the absorption in the K I 7699 Å line, as previously mentioned by Hein Bertelsen et al. (2016).

To determine the systemic velocity of MWC 137, we measured the central velocities of a sample of symmetric forbidden emission lines. We obtained an average radial velocity (RV) of 42.0 ± 0.6 km s^{-1}, which we used to correct all optical and infrared spectra.

Comparison of our spectra from different epochs revealed no obvious variability in the emission lines, neither in the Ondřejov spectra, which have a time difference of about two years, nor in the high-resolution FEROS spectra, which were taken about three months apart. Only a slight change in the profile of the Hα line was noted in the Ondřejov spectra. To compare with the FEROS data, we convolved the latter to the resolution of 13,000 of the Ondřejov spectra and confirm the earlier findings of Zickgraf (2003) that Hα is slightly changing over the years, as is shown in the upper-right panel of Figure 2. As the FEROS spectrum from 2016 has the highest quality, all following line profile figures refer to these data.

Most prominent are the emission lines from the Balmer series (Hα to Hδ; see Figure 2). The profiles of Hα to Hγ appear triple peaked. The wings of Hα, which extend to velocities of 3500–4000 km s^{-1} (bottom panel of Figure 2), are also remarkable. However, this high value is not a dynamic velocity. Instead, as for all B[e] supergiants, these wings are created by electron scattering. Zickgraf (2003) reported much smaller Hα wings with velocities reaching to only about half of our value. Such a drastic change in the wings might be caused by an increase in the number of scatterers, i.e., free electrons, along the line of sight, possibly due to a higher mass-loss rate.

Lines from the Paschen series are resolved up to Pa(30). Their profiles appear to be composite, consisting of a

[15] IRSA, http://irsa.ipac.caltech.edu.

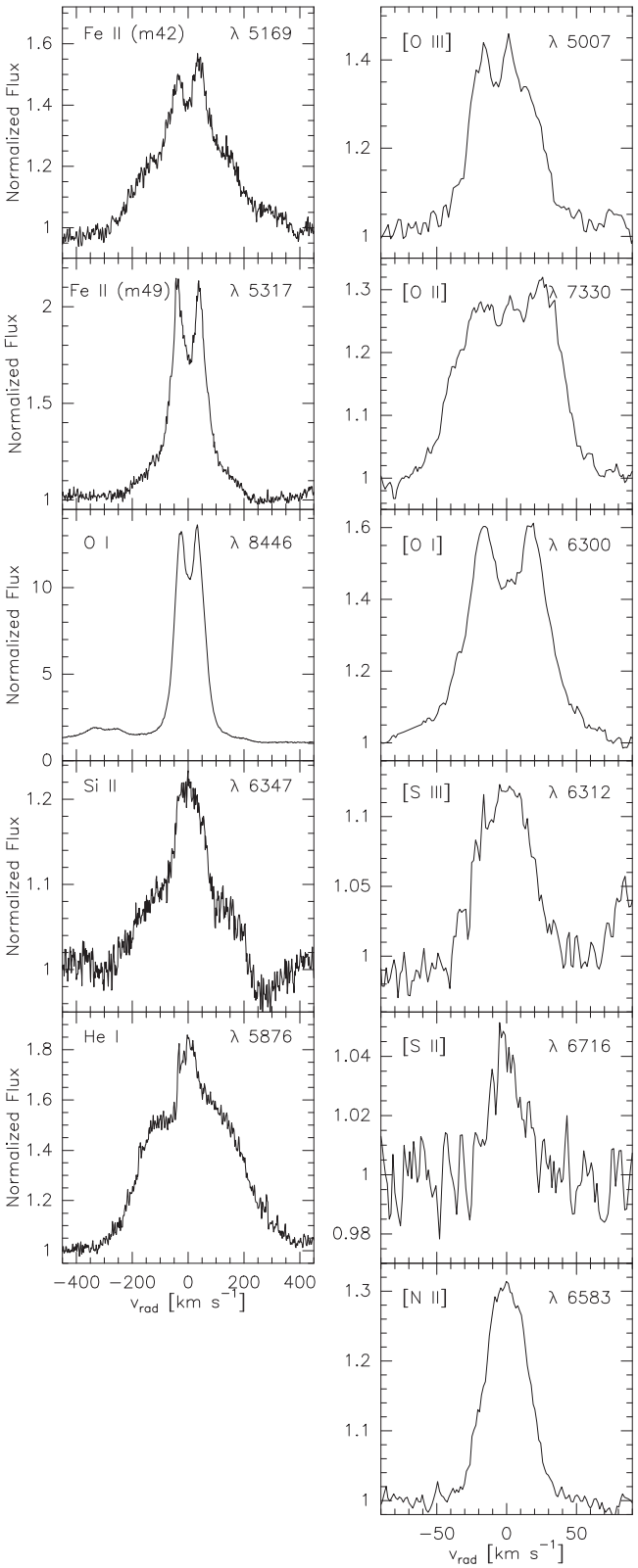

Figure 3. Line profile variety in (left) permitted and (right) forbidden lines in different ionization states.

symmetric double-peaked component with a peak separation of 65–70 km s^{-1} on a weak but broad component with wings extending up to ∼350 km s^{-1}, as shown for Pa(12), as an example, in Figure 2. The lines Pa(13), Pa(15), and Pa(16) are blended with the Ca II triplet lines. These calcium lines have double-peaked profiles, as was previously reported by Hamann & Persson (1992). Also included in this wavelength range are the O I λ8446 line and a few weak lines of Fe II and N I, all of which display double-peaked profiles. The full profile shape of the O I λ8446 line is shown in the middle-left panel of Figure 3. With a peak separation of ∼60 km s^{-1}, this line appears slightly narrower than the Paschen double peaks.

Profiles similar to the Paschen lines are observed for the Fe II lines. Example profiles from multiplets 42 and 49 are shown in Figure 3. The broad underlying component has clearly asymmetric line wings.

The lines of He I and Si II are similar to the lower Balmer line profiles with a triple-peaked structure (Figure 3). It is interesting to note that the triple-peaked profile in He I λ5876 was also seen in 2002, while older observations from 1987 revealed that this line was in absorption (Zickgraf 2003). This change from absorption to emission is an indicator for higher densities along the line of sight, in agreement with the broader electron scattering wings of Hα.

In contrast to the broad permitted lines, the profiles of the forbidden emission lines are typically much narrower and single peaked. The only exceptions are the lines [O I] λλ6300, 6364, which display clear double-peaked profiles (see Figure 3 for an example) with peak separations of 32–33 km s^{-1}. The lines of [O II] are typically blends. Their real profile shape is thus hidden. The coexistence of different ionization states of individual elements such as oxygen and sulfur is a clear hint for a nonspherical density distribution of the circumstellar material. In particular, the presence of lines from O I and O III is similar to the spectra seen from the compact planetary nebula Hen 2–90 (Kraus et al. 2005). In this object, optical imaging revealed a very hot polar wind in which the emission from twice-ionized elements such as O III arise, together with a cold equatorial disk from which the emissions from neutral atoms and dust originate.

A Keplerian rotating disk or ring scenario as the formation region of the double-peaked profiles of the [O I] lines was proposed for the B[e] supergiants (Kraus et al. 2010) and now seems to be well-established based on different (atomic and molecular) tracers (Aret et al. 2012; Cidale et al. 2012; Wheelwright et al. 2012; Kraus et al. 2015). The double-peaked [O I] lines might thus trace a compact disk around MWC 137.

Interestingly, we observe neither [O I] λ5577 nor [Ca II] λλ7291, 7324. As these lines are typically associated with the denser regions of the circumstellar disks closer to the star than the [O I] λλ6300, 6364 line-forming region (see, e.g., Kraus et al. 2010; Aret et al. 2012, 2016; Maravelias et al. 2017), the lack of observable emission in these lines suggests that the density in the cool, close-by environment of MWC 137 might be lower than in other B[e] supergiants.

The wings of most of the forbidden emission lines extend to velocities of about 50 km s^{-1}. Only the lines [N II] λλ6548, 6583 and [S II] λλ6716, 6731 are narrower (⩽30 km s^{-1}). Moreover, these lines are very weak in our spectra, whereas they become very intense in the large-scale nebula.

3.2. Kinematics of the Large-scale Optical Nebula

To investigate the nebula kinematics, we make use of long-slit spectra. The orientation and nebula coverage of the three available slit positions are presented in the left panel of Figure 4.

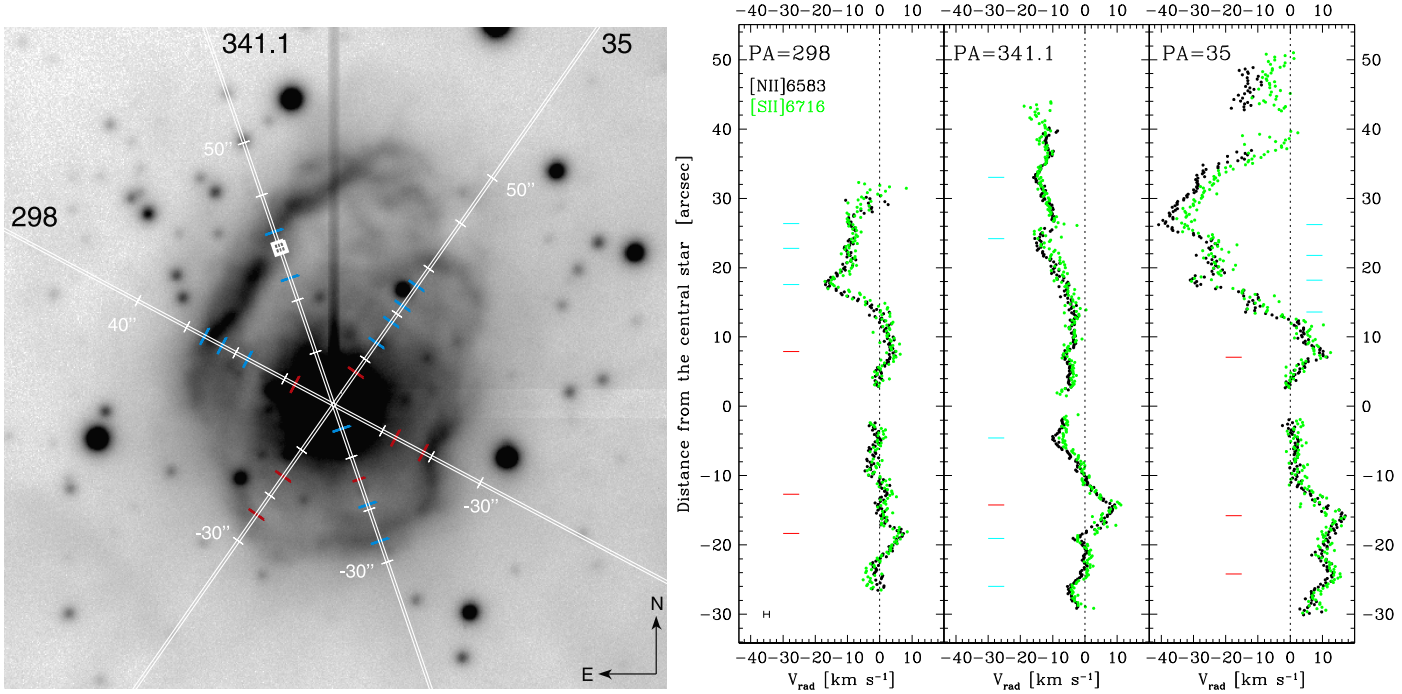

Figure 4. Left: positions of the NOT slits (white) and their PA values (black numbers) overlaid on the zoomed-in (FOV of $2' \times 2'$) ALFOSC Hα image. A distance scale in steps of $10''$ is marked with white ticks along the slits in both directions from the central star. Red and cyan ticks mark the positions of red- and blueshifted RV extrema, respectively. PA $= 341.^{\circ}1$ is along the jet, and the white square indicates knot c. Right: radial velocities of the [N II] 6583 Å (black) and [S II] 6716 Å (green) emission lines. Positive distance from the central star on the image is toward the north, negative toward the south. Red and cyan ticks mark the red- and blueshifted velocity extrema determined for the [N II] 6583 Å line. The average error bar for all of the measurements is in the lower-left corner.

Table 1
Radial Velocity Measurements

PA (°)	λ_{lab} (A)	RV (km s^{-1})	Error RV (km s^{-1})	Dist ($''$)
35	6716.44	3.85	0.90	−29.84
35	6716.44	5.23	0.90	−29.63
35	6716.44	11.03	0.90	−29.42
35	6716.44	8.27	0.90	−29.21
35	6716.44	9.83	0.90	−29.00

(This table is available in its entirety in machine-readable form.)

Table 2
Extrema of the RV Values of [N II] 6583 Å Marked in Figure 4

PA (°)	RV (km s^{-1})	Dist ($''$)
298	7.32	−18.36
	2.27	−12.69
	4.82	7.89
	−16.81	17.55
	−10.98	22.80
	−9.71	26.37
341.1	−5.41	−25.99
	−3.68	−19.06
	9.16	−14.23
	−10.01	−4.57
	−15.56	24.20
	−15.93	33.02
35	13.35	−24.20
	17.04	−15.80
	11.39	7.09
	−13.84	13.60
	−31.00	18.22
	−29.14	21.79
	−40.79	26.20

For the RV measurements, we used the two nebula lines, [N II] λ6583 and [S II] λ6716, because they are the more intense ones from the doublets. These lines can be traced from the stellar position out to the edges of the optical nebula. As the images are strongly saturated in Hα, in particular in the vicinity of the central star's position, this line was excluded from the analysis. The measurements were done from 2D spectra by fitting the line profiles line by line with a single Gaussian. Occasionally, a cosmic ray, which could not be removed, fell on top of the line. Also, in some parts of the nebula, the intensity was too weak for reliable measurements. These regions were thus excluded. The measurements were corrected for heliocentric and systemic velocities, and the resulting RV values along the three individual positionings of the slit are shown in the right panel of Figure 4. Full information on the final RVs is available in the machine-readable version of Table 1.

Both nebula lines display the same kinematic behavior, with RV values ranging from -41 to $+18$ km s^{-1}. The errors of the individual measurements are relatively small, on the order of 0.9 km s^{-1} on average as shown by the error bar in the lower-left corner of the RV plot. They were estimated based on the rms of the wavelength calibration, whereas the contribution from the fitting is negligible. Precise error values are included in Table 1.

The [S II] λ6716 line is considerably weaker than the [N II] λ6583 line, resulting sometimes in a larger scatter of the measured values, in particular in regions of lower intensity as is the case at the edges of the nebula structure and in the northern

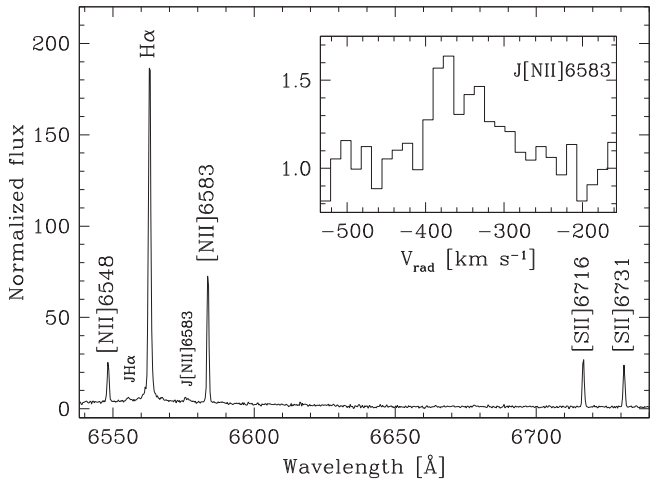

Figure 5. ALFOSC spectrum of the nebula emission and the emission of the jet component c (denoted J Hα and J [N II] 6583). The J [N II] 6583 line of knot c in the insert indicates a substructure over a large velocity range that was previously not reported.

region of PA = 35°. Along this position angle, the intensity in both lines basically disappears at distances 38″–42″ to the north so that the velocities could not be measured, resulting in a gap in Figure 4.

As a general trend, we note that emission from the northern nebula parts is predominantly blueshifted, whereas the southern regions have mostly redshifted emission. However, deviations from this general trend exist. For instance, the RV measurements for PA = 35° and PA = 298° display redshifted emission in the northern nebula part in the vicinity of the star (5″–15″). In addition, PA = 341.°1 displays three southern regions with blueshifted emission. In fact, we observe a series of extrema in the RV measurements along each slit position. They are marked by cyan and red ticks in both panels of Figure 4 and represent the maxima in blue- and redshifted velocities, respectively. These values are also listed in Table 2.

Most remarkable is the RV variation along PA = 35°. It displays the highest amplitudes in both blue- and redshifted emission while the slit passes through nebula regions that appear less intense. The blueshifted emission seen toward the north contains a series of pronounced maxima. The image of the nebula also shows that this region seems to have generally more structure. However, there is another star (identified as B3-5 by Mehner et al. 2016) in close vicinity of PA = 35° at a distance of ∼25″, which might influence the kinematics of the nebula.

Close inspection of the positions of the major velocity extrema along all three slits in comparison with the intensity structure of the nebula reveals that they typically precede intensity accumulations.

3.3. Jet

PA = 341.°1 was positioned such that it covered parts of the jet discovered by Mehner et al. (2016). As this jet appears slightly tilted (see their Figure 8) and the slit is rather narrow, only one clear signal from the jet is seen in our data: the emission from knot c. This feature is located at a distance of 30″ from the central star and is marked by a white box in Figure 4. On the 2D image, knot c has a slightly elongated shape spreading over about 10 × 10 pix. This size corresponds to 2.″1. We observe a clear inclination of the feature on the 2D image, meaning that the knot displays a velocity gradient with a smaller blueshift for larger distances from the star.

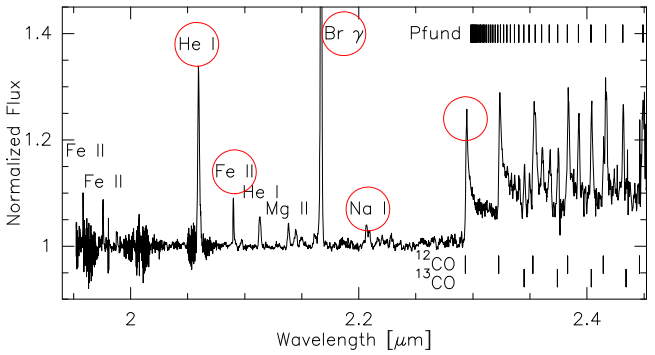

Figure 6. SINFONI *K*-band spectrum. Prominent emission features are marked. The blue region contains significant remnants from telluric pollution that could not be cleaned.

The intensity of the knot is too low to perform a line-by-line measurement of the velocities over the feature. Therefore, we added up the 10 lines in the spatial direction. The resulting nebula plus the knot c emission spectrum is shown in Figure 5. The jet emission is very faint and seen only in Hα and [N II] 6583 (labeled J Hα and J [N II] 6583 in the plot), while Mehner et al. (2016) also discovered it in the [N II] 6548 line and in the two [S II] lines in their long-exposure image. The strongest jet emission line is J [N II] 6583 from which we derive a mean knot RV of −356.5 km s^{-1}, in agreement with the estimates of Mehner et al. (2016) from their low-resolution spectra.[16]

A blow-up of the jet emission feature J [N II] 6583 is shown in the inset of Figure 5. It demonstrates that the line profile of knot c is rather broad and double peaked compared to the narrow, single-peaked regular nebula line. Considering the double-peaked profile shape in combination with the elongated inclined structure identified on the 2D image, we tend to believe that knot c might consist of at least two individual substructures. Fitting both with individual Gaussians, we obtain an RV of −378.9 km s^{-1} and FWHM of 25.4 km s^{-1} for the narrow blue component, and an RV of −334.0 km s^{-1} and FWHM of 55.9 km s^{-1} for the broad red component.

We note that no indication for either a blue- or a redshifted knot component could be identified in the FEROS spectra covering the innermost 2″.

3.4. Small-scale Structures in the Near-infrared

We now turn to the near-IR spectra that trace the circumstellar material in the vicinity of MWC 137. The full extracted *K*-band spectrum obtained with SINFONI is shown in Figure 6. It displays numerous emission features and prominent CO band emission. This molecular emission was first detected by Oksala et al. (2013), who observed MWC 137 with SINFONI using the largest spatial plate scale (8″ × 8″). The global spectral appearance in both SINFONI observations is practically identical. Based on high-resolution observations focused on the CO first overtone bands, Muratore et al. (2015) resolved the profile of the bandheads. Their intensities were found to display a blue shoulder and a red maximum, typical for rotating media. With the interpretation of the CO bands originating from a Keplerian disk around MWC 137, Muratore

[16] Note that Mehner et al. (2016) did not correct their measurements for systemic velocity.

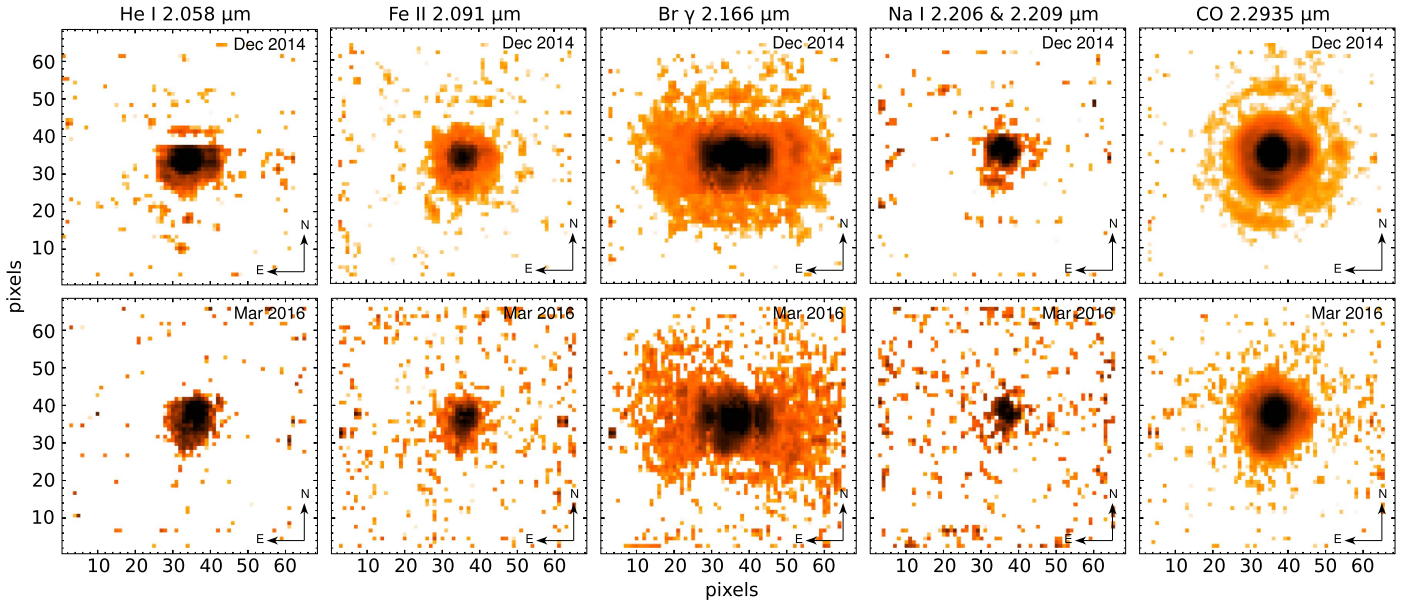

Figure 7. Spatial distribution of continuum-subtracted line emission of specific features. The top row shows the observations from 2014, and the bottom row those from 2016 for comparison. The image sizes are $0\farcs8 \times 0\farcs8$. To visualize the features, the display has been optimized individually for each panel.

et al. (2015) derived a rotation velocity, projected to the line of sight, of $v \sin i = 84 \pm 2$ km s^{-1}. This velocity is too small to be resolved with SINFONI.

With the IFU datacubes in the highest spatial resolution, we aimed to trace the spatial distribution of the circumstellar gas, and in particular of the hot molecular emission. Therefore, we investigated in more detail those individual emission features, which are marked by red circles in the *K*-band spectrum in Figure 6. For each line, we combined the individual slices from the datacube and subtracted a corresponding continuum image. The sodium lines are blended so we combined the emission from both lines into one image. As the red portion of the CO band emission is contaminated by Pfund line emission, we used only the non-polluted region around the first bandhead. The images of the continuum-subtracted emission observed in 2014 December and 2016 March are displayed for comparison in the top and bottom rows of Figure 7, respectively.

Starting with the data from 2014, we note that extended emission is seen in all of the lines, although the emission in the sodium lines appears to be weakest and concentrated around the stellar position. Brγ and CO have clearly structured emission patterns. The Brγ emission appears to be spread over a large volume, but mainly concentrated along the east–west direction with two prominent clumps east and west of the star and one toward the southeast. Additional minor, possibly arc-like structures appear north and south of these blobs, and a big circular shell-like structure with radius $\sim 0\farcs24$ might exist as well. A shell (or ring) of similar size is also visible in the CO image. Moreover, the CO emission displays three pronounced clumps seen to the east (least prominent), west, and southeast of the stellar position, which coincide pretty well with the structures seen in Brγ. In fact, the southeastern clump seems to be present (though weak) in the images of the other lines as well. The projected radial distances of these clumps range from $0\farcs092$ to $0\farcs118$.

The data from 2016 have much worse quality. Still, we see the extended emission in both Brγ and CO. There is one remarkable difference from the images from 2014: the clump to the southeast seems to have turned eastward by about 10° in a time span of just 15 months. This clump is again visible in the images of all investigated lines.

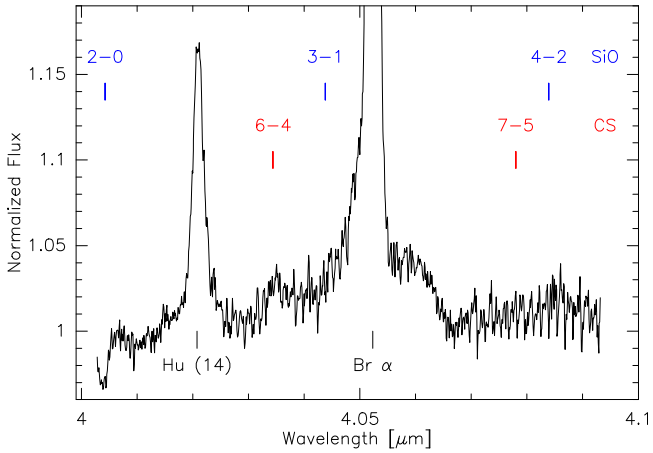

Figure 8. High-resolution GNIRS *L*-band spectrum with two prominent hydrogen recombination lines from the Brackett and Humphreys series. The bottom panel is a zoom on the continuum region. Wavelengths of the CS and SiO bandhead positions are marked but not clearly detected.

Although the spectral resolution of SINFONI is too low to resolve the kinematical broadening of the CO bands, one would still expect to see differences in the spectra extracted at individual pixels due to a temperature decrease of the CO gas from inside out. As the shape of the CO band spectrum, and in particular the relative strength of the individual bandheads, is sensitive to the gas temperature (see, e.g., Kraus 2009), the CO bands should look considerably different when extracted close to the star compared to those extracted at far distances. However, we find that the shapes of the CO band spectra are all identical, and also the normalized intensities are the same, independent of the position in the environment from which they were extracted. Such a behavior disagrees with the interpretation that the images display CO band emission originating from the environment of MWC 137. Instead, the

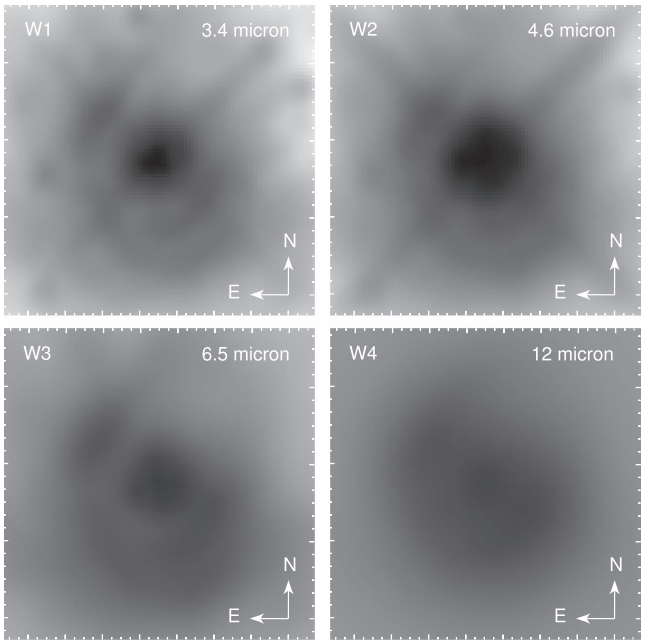

Figure 9. *WISE* images of MWC 137 in the four different bands. Image sizes are $2' \times 2'$.

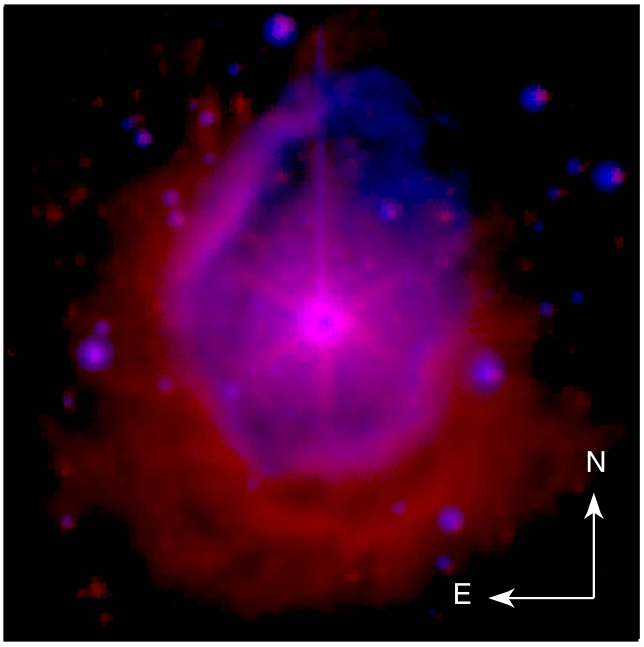

Figure 10. Composite image of the ALFOSC Hα (blue) and the *Spitzer* 3.6 μm (red) images. Image size is $2' \times 2'$.

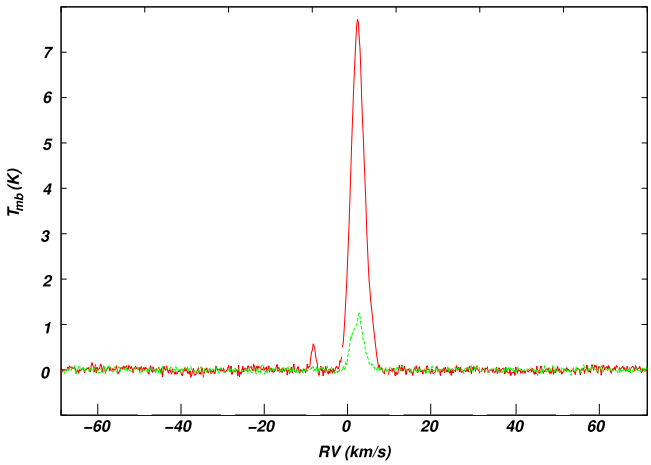

Figure 11. Averaged ^{12}CO(3–2) (red) and ^{13}CO(3–2) (green) spectra in units of the main-beam brightness temperature, $T_{\rm mb}$, obtained within the observed area.

emission we see appears to be light that was reflected by dust, and the clumpy structures we see are presumably dust concentrations around the central object. Support for such an interpretation comes from the images of the other emission features, which all display the same southeastern clump, independent of the ionization and excitation states of the element. The image of He I, which is also one of the strongest features in the spectrum, additionally displays the blobs east and west of the star. Brγ is the most intense spectral feature. Whether its image might be composite, i.e., consisting of reflected light and real emission from the ionized wind, or whether it is also just pure reflected light, is difficult to judge.

3.5. Other Hot Molecules

The infrared spectral range is the most ideal to search for emission from other molecules. In a pioneering study, Kraus et al. (2015) identified SiO band emission from a sample of four B[e] supergiants with confirmed CO band emission. These SiO bands arise in the 4 μm region around the Brα line. Our GNIRS spectrum is centered on the Brα position, which obviously dominates the spectrum. Also prominent is the emission from the hydrogen line Hu(14). To search for molecular features, we zoomed in to the continuum (Figure 8) and marked the bandhead positions of two molecules: SiO and CS. Unfortunately, this spectral region is strongly polluted by telluric features, which could not be satisfactorily removed, significantly hampering the proper identification of molecular bandhead structures. We computed a large grid of model spectra for both molecules but could not find any reasonable agreement with the features. We conclude that if present, the emission features from any of these molecules must be negligibly weak.

3.6. Circumstellar Dust

The presence of dust around MWC 137 is known from the recorded large infrared excess emission (Frogel et al. 1972; Cohen & Barlow 1975; Hillenbrand et al. 1992). However, not much is known about the spatial distribution of the dust. This can be investigated based on the numerous infrared images that were acquired in public surveys during the past few years.

MWC 137 was observed in all four *WISE* bands. The images are shown in Figure 9. Arc-like structures around the central star are resolved in all four bands. As the angular resolution of *WISE* drops significantly with increasing wavelength, this structure appears rather blurry at 12 μm. Extended emission of similar size and at a similar location is also seen in the far-infrared *Herschel* images acquired with PACS and SPIRE. The detectability of intense, extended emission up to 500 μm means that the ionized nebula of MWC 137 is surrounded by significant amounts of warm and cool dust. With the poor angular resolution of the far-infrared images, the emission appears blurry, similar to (or worse than) the W4 image shown in Figure 9, and we refrain from showing them here.

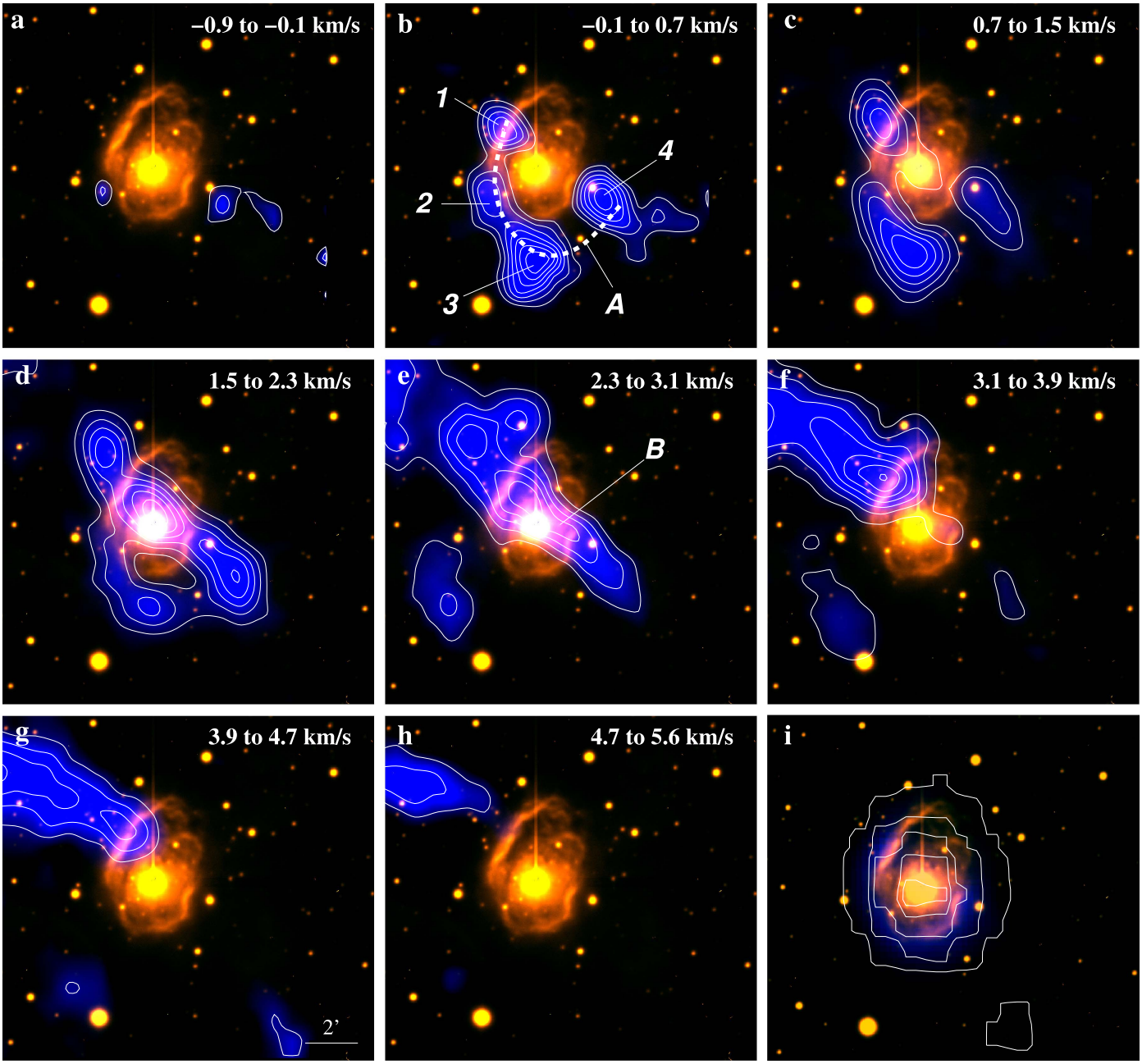

Figure 12. ^{13}CO(3–2) line emission distribution (in blue) in the velocity range from −0.9 to +5.6 km s^{-1} in steps of 0.8 km s^{-1}, superimposed on the ALFOSC Hα image (in orange). The numbers in panel (b) mark the position of the four clumps in Structure A. Velocity interval of each panel: (a) [–0.9, −0.1] km s^{-1}, (b) [−0.1, +0.7] km s^{-1}, (c) [+0.7, +1.5] km s^{-1}, (d) [+1.5, +2.3] km s^{-1}, (e) [+2.3, +3.1] km s^{-1}, (f) [+3.1, +3.9] km s^{-1}, (g) [+3.9, +4.7] km s^{-1}, and (h) [+4.7, +5.6] km s^{-1}. Contour levels for (a) and (b): 0.6 (3 rms) to 2.1 K in steps of 0.3 K; for (c) to (h): from 1.5 to 8.5 K in steps of 1.0 K. The last panel (i) displays an overlay of the *Herschel*-PACS emission at 70 μm (in blue) and the NVSS 1420 MHz radio continuum data (white contours at 0.01, 0.02, 0.03, 0.04, and 0.047 Jy/beam) on the Hα image.

It is noteworthy that the two images in W1 and W2 look very much alike. This finding is confirmed by the equal appearance of the two GLIMPSE survey images taken with much better angular resolution and sensitivity in the passbands IRAC-1 and IRAC-2 centered at 3.6 and 4.5 μm. Both bands cover specific but distinct emission features (e.g., Watson et al. 2008): IRAC-1/W1 covers the emission of PAHs at 3.3 μm, while IRAC-2/W2 covers emission from shocked molecular gas, such as H_2 lines and CO ro-vibrational transitions of the fundamental band as is found, for example, in the outflows of massive young stellar objects (Cyganowski et al. 2008) and/or emission of Brγ and Pfβ from ionized gas. Therefore, if either PAH emission or emission from shocked molecular gas/ionized gas were present in the nebula of MWC 137 and dominate the near-infrared appearance, the spatial distribution of the emission in these two bands should be physically disjoint. As this is not the case, we conclude that near-infrared emission structures most likely trace the spatial distribution of purely thermally emitting dust. The absence of shocked molecular gas is supplemented by the nondetection of H_2 emission lines in the *K*-band spectrum (see Figure 6).

Using high-quality near-infrared images, we can compare the spatial extent of both dust and ionized gas. Figure 10 shows a composite image of GLIMPSE 3.6 μm (red) and ALFOSC Hα

Table 3
Parameters of the Cold Molecular Gas

Structure	$T^p_{^{12}CO}$ (K)	$T^p_{^{13}CO}$ (K)	T_{exc} (K)	τ_{13}	T_{mean} (K)	Δv (km s^{-1})	$N_{^{13}CO}$ (10^{15}cm^{-2})	N_{H2} (10^{21}cm^{-2})	$R_1 \times R_2$ ($''$)	M_{H2} ($M_\odot$)
A-1	18.4	4.3	25.8	0.26	1.11	2.4	1.46	1.1	31 × 21	35
A-2-3	14.5	2.8	21.7	0.21	1.64	2.2	2.03	1.6	48 × 25	85
A-4	14.0	3.1	21.2	0.25	0.94	1.8	0.98	0.8	21	15
B-southern	18.0	3.3	25.4	0.20	1.09	4.4	3.37	2.6	40 × 25	120
B-northern	15.0	3.5	22.2	0.26	2.16	4.4	5.47	4.2	39 × 34	245

(blue). Comparison of the near-infrared emission to the optical one reveals that the dust emission is basically encircling the optical nebula, following the wiggly structure of the optical filaments. However, we note two significant differences. There is no dust emission toward the northwest direction. Moreover, in the south, the dust emission displays an additional arc-like structure, which has no optical counterpart. This additional dust arc appears at a distance of about 40″ and is hence 10″–15″ (from south to southwest) farther out than the optical southern filament.

3.7. Cold Molecular Gas

We turn now to the description of the radio data. These contain information on the cold molecular gas at distances far from the star.

The ^{12}CO(3–2) and ^{13}CO(3–2) spectra averaged within a 3′×3′ region centered on R.A.(J2000) = $6^h18^m45\overset{s}{.}5$ and Decl. (J2000) = +15°16′52.″3 are shown in Figure 11. The molecular emission accumulates in one bright component between −2 and +8 km s^{-1} as detected in the ^{12}CO(3–2) data, and between −1.0 and +5.8 km s^{-1} in the ^{13}CO(3–2) emission. A very faint component detected at −8 km s^{-1} in ^{12}CO(3–2) has no clear relation to the nebula and will be ignored in the present analysis. No obvious signal was detected in either the SiO(5–4) or CS(5–4) molecular lines.

3.7.1. Spatial Distribution

The structures seen in the two CO isotopes are generally the same, with the ^{12}CO(3–2) emission slightly more extended than the ^{13}CO(3–2) emission due to the presence of low-intensity diffuse gas. But since the ^{12}CO(3–2) emission is optically thick, it provides limited information on the internal structure and dynamics of the molecular gas. Therefore, we focus on ^{13}CO(3–2) and integrate the emission in the velocity interval [−0.9, +5.6] km s^{-1}, in steps of 0.8 km s^{-1}. The distribution of the emission within these velocity bins is displayed in Figure 12. The emission is concentrated at and around the eastern, southern, and southwestern borders of the optical nebula and is in perfect alignment with the spatial distribution of the dust identified in the near- and mid-IR (see Figure 9). As with dust, there is an obvious lack of molecular gas toward the northwest, coincident with the region of largest negative nebular velocities at PA = 35° (see Figure 4).

We detect two extended structures toward the nebula. The first one (henceforth Structure A) is present in the velocity range [−0.1, +1.9] km s^{-1} (panels (b) to (d)) and encircles the eastern and southern optical rims. This structure is subdivided into four molecular clumps as clearly seen from panel (b). Comparison with the optical images shows that clump 1 coincides with a bright optical filament, while clumps 2 and 3 have their emission peaks to the southeast and south of, but outside, the optical nebula. These latter two clumps (2 and 3) merge into an arc-like structure at higher velocities (see panels (c) and (d)). The center of clump 3 coincides with the additional arc-like structure mentioned in the last paragraph of Section 3.6. A fourth clump (4) closely borders the brightest optical filament to the west. The spatial correlation of this partial ring-like structure and the Hα emission strongly suggests that material at these velocities corresponds to the molecular counterpart of the optical nebula.

The second configuration (Structure B) is an elongated feature that runs across the nebula in the northeast–southwest direction (PA ≃ 310°; panels (d) to (f)), approximately perpendicular to the major axis of the elongated optical nebula. The entire structure is detected from +3.9 km s^{-1} down to +1.5 km s^{-1}, where it breaks apart and ends up in clumps 1 and 4. The regions of maximum intensity in Structure B coincide with the brightest domains in the filaments of the optical nebula Sh 2-266. The northeastern part of Structure B is still visible in the velocity interval [+4.1, +5.5] km s^{-1} (panels (g) and (h)), which is just a bit higher. Considering the huge spatial extent of this whole elongated feature, which displays only a small variation in velocities, we might conclude that Structure B encloses a rather small angle with the plane of the sky.

A comparison of the 70 μm emission detected by *Herschel*-PACS is displayed in panel (i) of Figure 12. It demonstrates that the far-IR emission of the cold dust coincides[17] with the molecular emission, providing a link between dust and molecular gas in the two Structures A and B.

3.7.2. Physical Parameters of the Molecular Components

We evaluate the physical parameters of the two identified structures separately, although they are partially superposed in velocity and in space. For the arc-like Structure A that surrounds Sh 2-266, we consider the ^{13}CO emission separately for clump 1, clumps 2 plus 3, and clump 4. For the elongated Structure B, we individually derive the values for the northern and southern sections.

Assuming Local Thermodynamic Equilibrium (LTE) conditions and that the emission in the ^{12}CO line is optically thick, we compute the excitation temperature T_{exc} from the emission in the ^{12}CO(3–2) line. Using the relation

$$T^p_{^{12}CO}\ [\mathrm{K}] = T^*_{^{12}CO}\ [J_{12}(T_{exc}) - J_{12}(T_{bg})] \quad (1)$$

for the peak main-beam brightness temperature ($T^p_{^{12}CO}$) of the ^{12}CO line, where $T^*_{^{12}CO} = h\nu_{12}/k$ with the frequency ν_{12} of the ^{12}CO(3–2) line, $J_{12}(T) = (e^{T^*_{^{12}CO}/T} - 1)^{-1}$, and T_{bg} is the background temperature, for which we use the value of 2.7

[17] We note that the emission at 160μm (not shown) is slightly more extended.

K, the excitation temperature for this CO line results in

$$T_{\rm exc}\ [{\rm K}] = \frac{16.59}{\ln\,[1\ +\ 16.59/(T^{p}_{12{\rm CO}}\ +\ 0.036)]}. \quad (2)$$

The values for $T^{p}_{12{\rm CO}}$ are thereby individually measured for the different clumps and structures from the averaged spectra.

The optical depth τ_{13} was obtained from the ^{13}CO(3–2) line using the expression

$$\tau_{13} = -\ln\left[1 - \frac{T^{p}_{13{\rm CO}}}{T^{*}_{13{\rm CO}}}[J_{13}(T_{\rm exc}) - J_{13}(T_{\rm bg})]^{-1}\right], \quad (3)$$

where $T^{*}_{13{\rm CO}} = h\nu_{13}/k$ with the frequency ν_{13} of the ^{13}CO(3–2) line, and $J_{13}(T) = (e^{T^{*}_{13{\rm CO}}/T} - 1)^{-1}$. For this derivation, we assumed that the excitation temperature for the ^{13}CO emission line is the same as for the ^{12}CO line. The ^{13}CO line ($T^{p}_{13{\rm CO}}$) peak main-beam brightness temperatures for the clumps in Structure A and for the northern and southern sections of Structure B were also obtained from the averaged spectra within the emitting regions. The peak and excitation temperatures, and optical depths are summarized in columns 2, 3, 4, and 5 of Table 3.

Assuming LTE, the ^{13}CO column density, $N_{13{\rm CO}}$ [cm^{-2}], can be estimated from the ^{13}CO(3–2) line following Buckle et al. (2010),

$$N_{13{\rm CO}} = 8.3\ \times\ 10^{13} e^{15.87/T_{\rm exc}} \frac{T_{\rm exc} + 0.88}{1\ -\ e^{-15.87/T_{\rm exc}}} \int \tau_{13} dv. \quad (4)$$

The integral in Equation (4) can be approximated by

$$\int \tau_{13} dv = \frac{1}{T^{*}_{13{\rm CO}}[J(T_{\rm exc}) - J(T_{\rm bg})]} \frac{\tau_{13}}{1\ -\ e^{-\tau_{13}}} \int T_{\rm mb}\ dv, \quad (5)$$

with

$$\int T_{\rm mb}\ dv = T_{\rm mean} \Delta v. \quad (6)$$

Equation (5) is appropriate to eliminate small optical depth effects and is good within 15% for the derived values of τ_{13} (Rohlfs & Wilson 2004). Bearing in mind the τ_{13} values listed in Table 3, the correction increases the optically thin column density by about 10%–15%. $T_{\rm mb}$ and $T_{\rm mean}$ in Equation (6) are the main-beam and the averaged brightness temperature of the ^{13}CO(3–2) line, and Δv is the velocity interval of the emitting areas. For the arc-like Structure A that surrounds Sh 2-266, we consider the ^{13}CO emission within the velocity interval [−0.9, +1.5] km s^{-1} (panels (a) to (c) in Figure 12) for clump 1, [−0.3, +2.1] km s^{-1} (panels (a) to (d)) for clumps 2 and 3, and [−0.9, +0.9] km s^{-1} (panels (a) to (c)) for clump 4. For the elongated Structure B, we take into account the emission in the velocity range [+0.9, +5.7] km s^{-1} and derive the values for the northern and southern sections.

The molecular mass was calculated using

$$M_{\rm H2}\ [{\rm g}] = \mu\ m_{\rm H}\ A\ N_{\rm H2}\ d^{2}, \quad (7)$$

where μ is the mean molecular weight, which is assumed to be equal to 2.72 after an allowance of the relative helium abundance of 25% by mass (Yamaguchi et al. 1999), $m_{\rm H}$ is the atomic hydrogen mass, and $N_{\rm H2}$ is the H_2 column density, obtained using an abundance ratio $N_{\rm H2}/N_{13{\rm CO}} = 7.7\ \times\ 10^{5}$ (Wilson & Rood 1994). A is the solid angle of the CO-emitting regions, obtained from the semi-axis $R_1\ \times\ R_2$ of the regions, and d is the distance to the star.

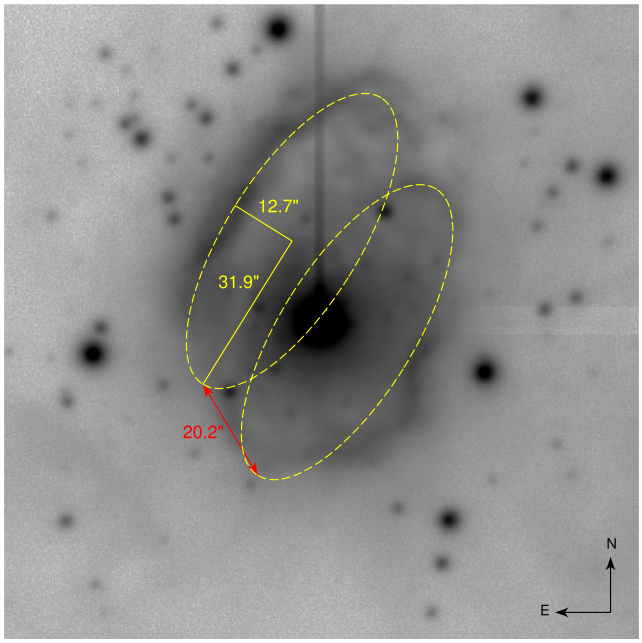

Figure 13. Measured quantities of the putative double-ring (or cone) structure of the optical nebula. The image size is 2″ × 2″.

The distance to the molecular gas around Sh 2-266 can be estimated from the velocity field of the outer Galaxy, which was derived by Brand & Blitz (1993). Considering a mean RV of −0.5 km s^{-1} of Structure A (corresponding to an LSR velocity of +27.5 km s^{-1}), we find a kinematical distance $d \geqslant 5.5$ kpc. This distance is similar to the spectroscopic distance toward the nebula, for which Mehner et al. (2016) determined a value of 5.2 ± 1.4 kpc, and we adopted the spectroscopic value of 5.2 kpc for our computation of the molecular mass. Uncertainties in the molecular masses are about 50% and originate mainly from the distance uncertainties.

The summary of our results is presented in Table 3, where we list the average main-beam brightness temperature ($T_{\rm mean}$, column 6), the velocity interval (Δv, column 7), the column densities of ^{13}CO and H_2 (columns 8 and 9), the semi-axis of the emitting area ($R_1\ \times\ R_2$, column 10), and the molecular mass ($M_{\rm H2}$, column 11). The huge values found for the molecular masses imply that the cold material surrounding MWC 137 must be interstellar in origin.

Finally, we compute the volume density $n_{\rm H2}$. This is not an easy task since it involves the geometry and volume of the structures. A rough estimate of this parameter for the clumps in Structure A adopting the semi-axis listed in Table 3 indicates values in the range 400–660 cm^{-3}. For Structure B, we adopt an elongated ellipsoid including the northern and southern sections and find a volume density of 1200 cm^{-3}. Uncertainties in these values are about 70%. The relatively low volume densities are compatible with the nondetection of high-density tracers, such as the CS molecule.

3.8. Ionized Gas

Similar to the Hα image, the radio continuum emission at 1.4 GHz indicates the presence of ionized gas (Figure 12). The image acquired during the NVSS survey reveals a centrally

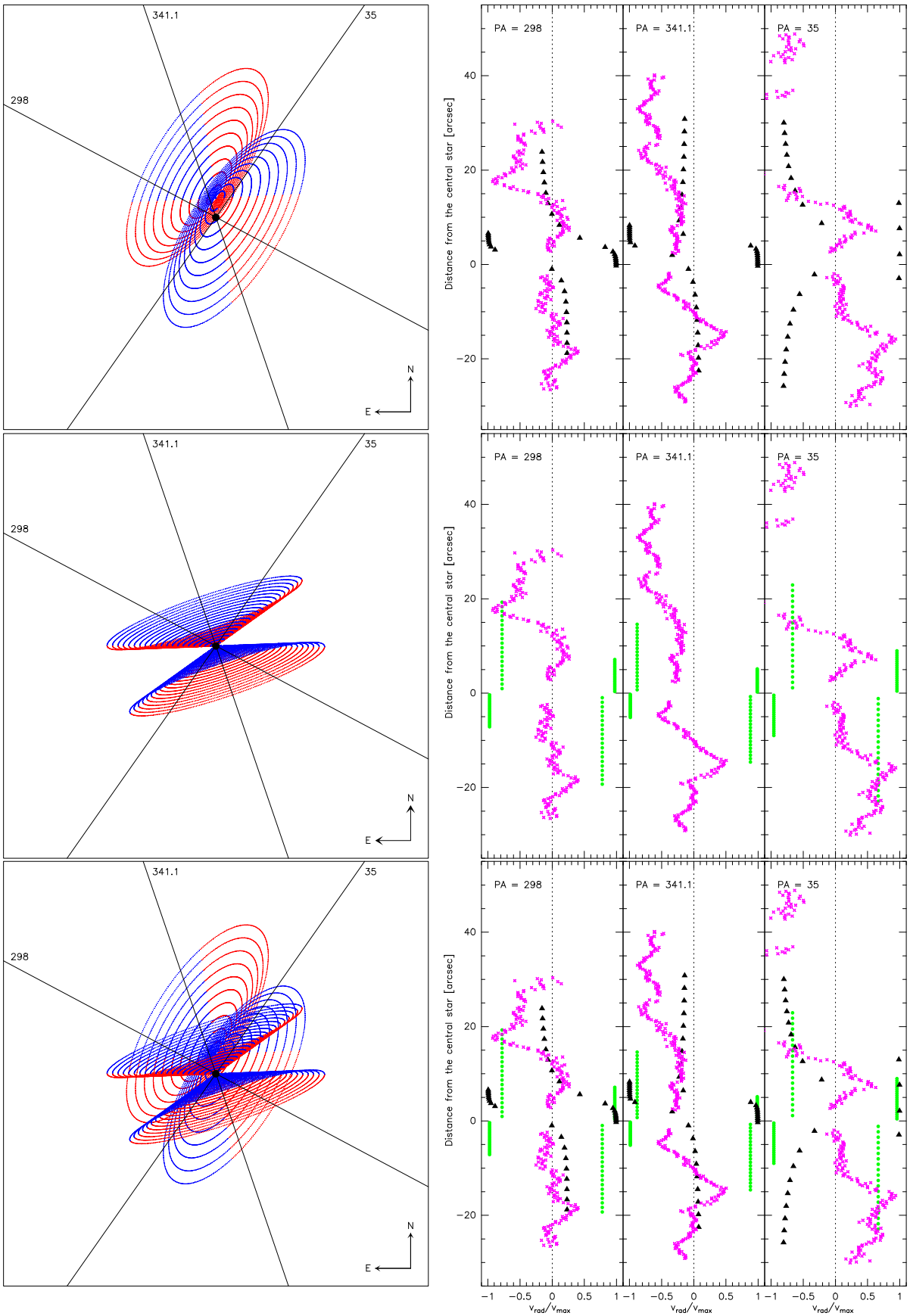

Figure 14. Left: nebula kinematics for the scenario of a sheared double-cone structure as estimated from the optical nebula (top), for a regular double cone centered on the stellar position and with the jet PA as symmetry axis (middle), and a combination of both (bottom). In both cases, the northeastern cone points away from and the southwestern one points toward the observer. Colors indicate regions with blue- and redshifted velocities. Image size corresponds to $2'' \times 2''$. Right: model kinematics along the PAs (black triangles and green dots) compared to observations (purple crosses).

peaked source coinciding with Sh 2-266, with a flux density $S_{1.4\,\mathrm{GHz}} = 78$ mJy.

The number of Lyman continuum photons needed to maintain the ionization of the H II region can be calculated from the 1.4 GHz emission using

$$N_{\mathrm{Lyc}}\ [\mathrm{s}^{-1}] = 7.58 \times 10^{48}\ T_{\mathrm{e}}^{-0.5}\ S_{1.4\,\mathrm{GHz}}\ d^2 \qquad (8)$$

(Kurtz et al. 1994). Adopting an electron temperature of 10^4 K, we estimate $N_{\mathrm{Lyc}} = 1.6 \times 10^{47}\ \mathrm{s}^{-1}$. Assuming that about 50% of the UV photons are absorbed by interstellar dust in the H II region (Inoue 2001), a Lyman continuum flux of $3.2 \times 10^{47}\ \mathrm{s}^{-1}$ is necessary. This value should be easily provided by a B0.5I star, with a UV photon flux of $4 \times 10^{47}\ \mathrm{s}^{-1}$ (Smith et al. 2002). Bearing in mind the presence of a stellar cluster in the center of the nebula (Mehner et al. 2016), this value could be a lower limit.

4. Discussion

The optical nebula displays some structure that might be approximated by a double ring. This is visualized by the two identical, parallel ellipses overlaid on the ALFOSC image in Figure 13. We measured the semimajor ($a = 31\farcs9 \pm 1\farcs0$) and semiminor ($b = 12\farcs7 \pm 0\farcs5$) axes, the alignment of the ellipses (here, of the semiminor axis $\mathrm{PA}(b) = 328\fdg90 \pm 0\fdg50$), the distance ($c = 20\farcs2 \pm 0\farcs2$) between the two ellipses, and the alignment of the line connecting the two ellipses ($\mathrm{PA}(c) = 301\fdg89 \pm 0\fdg50$).

The equal dimensions of the ellipses and their parallel arrangement suggest that they might represent the outer rims of a double cone. However, since the alignment of the semiminor axis is not parallel to the alignment of the line connecting the two ellipses, this double cone must be sheared in one direction.

To test whether such a structure might be a reasonable scenario to explain the observed nebula kinematics, we use the observed parameters as constraints and compute the geometric shape of a sheared double cone. We start by defining a double cone in the north–south direction, which we align with the z-axis. The top and bottom circles have radius R, which is given by the length of the semimajor axis a of the ellipse. The height of each cone is h so that the object extends from $z = -h$ to $z = +h$, and the angle α represents half the opening angle of the cone. Then, we apply a shear Δy along the y-axis. This shear is characterized by the angle ξ defined via $z = \Delta y \tan \xi$. Finally, we rotate the double cone first around the y-axis with angle θ and then around the z-axis with angle ϕ, where θ and ϕ represent the usual spherical coordinates. This rotated double-cone structure is then projected onto the y–z plane, which we identify with the plane of the sky.

To compute the kinematics, we assume that the gas is streaming radially with constant velocity and purely along the cone surfaces. This allows us to determine the regions of blue- and redshifted emission. To reproduce the observed quantities and position angles, we found the values of $h = 17\farcs81$, $\alpha = 60\fdg86$, and $\xi = 137°$ for the double-cone parameters, and $\theta = 119°$ and $\phi = 63°$ for the rotation angles. The projection of this geometrical shape onto the plane of the sky is shown in the top-left panel of Figure 14. In blue and red we mark the regions with blue- and redshifted gas kinematics, respectively.

Next, we overlaid the position angles of the slits and determined the intersection points with the projected double cone. During the observations, the three PAs were positioned such that they intersect at the location of the star. However, with respect to the chosen geometrical model, it is important to note that the center of the double cone was found to be located $5\farcs5$ north of the stellar position. The extracted velocity values at the intersection points, normalized to the constant outflow velocity, are shown in the top-right panel of Figure 14. For comparison, we included the observed velocities, which we normalized arbitrarily.

In the northern nebula regions, our model produces blueshifted emission in agreement with the observations. Also, the redshifted northern emission in the vicinity of the star along $\mathrm{PA} = 298°$ agrees with the model predictions. Note that the densely populated regions at distances $0''$–$10''$ north of the star along $\mathrm{PA} = 298°$ and $\mathrm{PA} = 341\fdg1$ with both high blue- and redshifted velocities originate from the overlap regions of the two cones. What cannot be reproduced is the variability in the velocities and the high amplitudes observed in the blueshifted gas. In the southern nebula, our model produces redshifted emission. There is some agreement with the observations along $\mathrm{PA} = 298°$ and $\mathrm{PA} = 341\fdg1$; however, for $\mathrm{PA} = 35°$, the observations display strong redshifted emission in contrast to the theoretical predictions.

Although some of the kinematics can be reproduced, we are aware that the chosen geometrical scenario is too simple to account for all observed features. Still, this exercise provides important insight. The fact that the star MWC 137 is not located in the center of the geometrical double-ring structure suggests that the large-scale optical nebula was most probably not formed exclusively by the wind of a single star but rather by the combined winds of the early-type stars identified by Mehner et al. (2016) in the center of the cluster and in the vicinity of MWC 137. In addition, the jet, which was found by Mehner et al. (2016) to originate from MWC 137, is not aligned with the axis of the double cone. Instead, the jet is perpendicular to the circumstellar disk of MWC 137, which is traced by the intrinsic polarization in Hα (Oudmaijer & Drew 1999) and the rotationally broadened CO bands (Muratore et al. 2015). Under the presence of a circumstellar disk, the current wind of MWC 137 is most likely also channelled into a double cone, but with a different orientation. One might speculate whether this inner disk and the jet might point toward MWC 137 having a compact companion as, e.g., in the case of CI Cam (see, e.g., Clark 2006). The detection of an X-ray source in the vicinity of MWC 137 by Evans et al. (2014) might support such a suggestion. However, the uncertainty in the position of the X-ray source renders it difficult to unambiguously identify MWC 137 as the optical counterpart.

Unfortunately, the optical image provides no clear indication of the postulated second double cone, which might imply a (much) lower wind density. Besides the position angle of the jet and the request that the velocity in the southern part of the slit $\mathrm{PA} = 35°$ should be redshifted, we have no additional observational constraints for a possible model. Therefore, and simply for demonstration purposes, we compute a circular double cone centered on the star's position. To align it with the PA of the jet, we only altered the rotation angle θ, for which we find a value of 159° but kept the same value for ϕ. For the height and the cone opening angle, we adopted values of $10''$ and 71°. They were chosen such that the double-cone remains small but wide enough to guarantee predominantly redshifted emission in the southern intersection region with $\mathrm{PA} = 35°$.

The velocities were again computed under the assumption of a purely radial outflow along the cone surfaces.

The projection to the plane of the sky and the velocities along the slit positions are shown in the middle panels of Figure 14. As before, the northern cone points away from and the southern one toward the observer. The symmetric intersections with the slit positions and the chosen constant outflow velocity result in symmetric patterns of constant values in both red- and blueshifted velocities. Also, with this model, some of the observed features might be reproduced.

Finally, we combine these two double cones and present their projection and velocities in the bottom panels of Figure 14. Obviously, various observed features might be better reproduced with these combined double cones, while others still cannot be reproduced. This example shows that the real physical scenario is much more complex than what can be explained by our simplistic model. However, without further constraints from observations, it will not be possible to reconstruct a reliable scenario.

5. Conclusions

We performed a multiwavelength study of the evolved Galactic B[e] star MWC 137 and its gaseous environment on both large and small scales. Measuring the kinematics of the forbidden lines in the optical nebula results in the general trend that the northern part is approaching us while the southern region is receding. Approximating the double-ring structure apparent in the optical nebula by a sheared double cone, it is obvious that MWC 137 is not residing in the center of this geometrical pattern. Also, the axis of the double cone is not aligned with the jet axis. We conclude from this that MWC 137 alone cannot have formed and shaped the large-scale nebula. However, a second double-cone structure with its symmetry axis aligned with the observed jet and centered on the star's position might be postulated. Such a combined scenario provides many consistencies with the observed nebula kinematics.

Knot c of the northern jet, which displays a substructure and a velocity gradient in agreement with the general jet behavior, was resolved as well: the RV decreases with increasing distance from the star.

The large-scale distributions of the cold molecular gas and dust were also investigated. The molecular gas was mapped in the CO(3–2) lines, and we identified primarily two major groupings. The first one consists of four pronounced clumps northeast, east, south, and southwest of the optical nebula, forming an arc-like structure. The second large-scale structure is best described by a huge and more or less straight molecular belt spreading from the northeast to the southwest. As the velocity within this arrangement is confined to a very narrow range, it is most likely aligned with the plane of the sky. Since the kinematics at the outskirts of the optical nebula also agree with those of the molecular gas, we conclude that the cold gas is the remnant of the initial molecular cloud from which the cluster has formed. Support for this scenario is provided by the huge molecular masses that are inconsistent with material ejected during the previous evolution of one (or more) star(s).

The dust mapped in the near- and far-infrared surrounds the optical nebula in the same way as the cold molecular gas. It displays an additional arc toward the south, which is aligned with the southern arc of the cold molecular gas but which has no optical counterpart. No dust and cold gas are seen toward the north and the northwest of the optical nebula.

Dust clumps are also present on much smaller scales, in the vicinity of the star where they reflect the light coming from the innermost region, in which a circumstellar gas disk is expected to revolve around the star on Keplerian orbits. This gas disk gives rise to the rotationally broadened CO bands that are seen in the *K*-band and might also host the driving mechanism for the jet.

We thank the anonymous referee for constructive comments. This research made use of the NASA Astrophysics Data System (ADS) and of the SIMBAD database, operated at CDS, Strasbourg, France. We wish to thank Eero Vaher for the preparation of the Python script for datacube assembling. We also thank Moorits Mihkel Muru, Grete-Lilijane Küppas, and Gutnar Leede for collecting the NOT-ALFOSC spectra during the NOT course in 2016 November at Tuorla Observatory, University of Turku, Finland. Parts of the observations obtained with the MPG 2.2 m telescope were supported by the Ministry of Education, Youth and Sports project—LG14013 (Tycho Brahe: Supporting Ground-based Astronomical Observations). Parts of the data presented here were obtained with ALFOSC, which is provided by the Instituto de Astrofisica de Andalucia (IAA) under a joint agreement with the University of Copenhagen and NOTSA. M.K. and D.H.N. acknowledge financial support from GAČR (grant numbers 17-02337S and 16-05011S). The Astronomical Institute Ondřejov is supported by project RVO:67985815. T.L. acknowledges support from the institutional research funding IUT40-1 of the Estonian Ministry of Education and Research. This research was also supported by the European Union European Regional Development Fund, project "Benefits for Estonian Society from Space Research and Application" (KOMEET, 2014–2020. 4. 01. 16-0029). L.C., M.L.A., C.E.C., and N.D. acknowledge financial support from CONICET (PIP 0177 and 0356) and the Universidad Nacional de La Plata (Programa de Incentivos G11/137 and G11/139). Financial support for International Cooperation of the Czech Republic and Argentina (AVCR-CONICET/14/003) is acknowledged. L.C. and M.C. are grateful for the support from the project CONICYT + PAI/Atracción de capital humano avanzado del extranjero (folio PAI80160057). G.M. acknowledges support from CONICYT, Programa de Astronomía/PCI, FONDO ALMA 2014, Proyecto No 31140024.

ORCID iDs

Michaela Kraus https://orcid.org/0000-0002-4502-6330
Dieter H. Nickeler https://orcid.org/0000-0001-5165-6331

References

Aret, A., Kraus, M., Muratore, M. F., & Borges Fernandes, M. 2012, MNRAS, 423, 284
Aret, A., Kraus, M., & Šlechta, M. 2016, MNRAS, 456, 1424
Benjamin, R. A., Churchwell, E., Babler, B. L., et al. 2003, PASP, 115, 953
Berrilli, F., Corciulo, G., Ingrosso, G., et al. 1992, ApJ, 398, 254
Bonnet, H., Abuter, R., Baker, A., et al. 2004, Msngr, 117, 17
Brand, J., & Blitz, L. 1993, A&A, 275, 67
Brandner, W., Grebel, E. K., Chu, Y.-H., & Weis, K. 1997, ApJL, 475, L45
Buckle, J. V., Curtis, E. I., Roberts, J. F., et al. 2010, MNRAS, 401, 204
Churchwell, E. & GLIMPSE Team 2001, BAAS, 33, 821
Cidale, L. S., Borges Fernandes, M., Andruchow, I., et al. 2012, A&A, 548, A72

Clark, J. S. 2006, in ASP Conf. Ser. 355, Stars with the B[e] Phenomenon, ed. M. Kraus & A. S. Miroshnichenko (San Francisco, CA: ASP), 269
Cohen, M., & Barlow, M. J. 1975, ApL, 16, 165
Condon, J. J., Cotton, W. D., Greisen, E. W., et al. 1998, AJ, 115, 1693
Cyganowski, C. J., Whitney, B. A., Holden, E., et al. 2008, AJ, 136, 2391
Eisenhauer, F., Abuter, R., Bickert, K., et al. 2003, Proc. SPIE, 4841, 1548
Ekström, S., Georgy, C., Eggenberger, P., et al. 2012, A&A, 537, A146
Esteban, C., & Fernandez, M. 1998, MNRAS, 298, 185
Evans, P. A., Osborne, J. P., Beardmore, A. P., et al. 2014, ApJS, 210, 8
Fazio, G. G., Hora, J. L., Allen, L. E., et al. 2004, ApJS, 154, 10
Finkenzeller, U., & Mundt, R. 1984, A&AS, 55, 109
Frogel, J. A., Persson, S. E., & Kleinmann, D. E. 1972, ApL, 11, 95
Griffin, M. J., Abergel, A., Abreu, A., et al. 2010, A&A, 518, L3
Güsten, R., Nyman, L. Å, Schilke, P., et al. 2006, A&A, 454, L13
Hamann, F., & Persson, S. E. 1992, ApJS, 82, 285
Hein Bertelsen, R. P., Kamp, I., van der Plas, G., et al. 2016, A&A, 590, A98
Herbig, G. H., & Kameswara Rao, N. 1972, ApJ, 174, 401
Hernández, J., Calvet, N., Briceño, C., Hartmann, L., & Berlind, P. 2004, AJ, 127, 1682
Hillenbrand, L. A., Strom, S. E., Vrba, F. J., & Keene, J. 1992, ApJ, 397, 613
Inoue, A. K. 2001, AJ, 122, 1788
Kaufer, A., Stahl, O., Tubbesing, S., et al. 1999, Msngr, 95, 8
Kraus, M. 2009, A&A, 494, 253
Kraus, M., Borges Fernandes, M., & de Araújo, F. X. 2010, A&A, 517, A30
Kraus, M., Borges Fernandes, M., de Araújo, F. X., & Lamers, H. J. G. L. M. 2005, A&A, 441, 289
Kraus, M., Oksala, M. E., Cidale, L. S., et al. 2015, ApJL, 800, L20
Kurtz, S., Churchwell, E., & Wood, D. O. S. 1994, ApJS, 91, 659
Maravelias, G., Kraus, M., Aret, A., et al. 2017, in ASP Conf. Ser. 508, The B[e] Phenomenon: Forty Years of Studies, ed. A. Miroshnichenko et al. (San Francisco, CA: ASP), 213
Marston, A. P., & McCollum, B. 2008, A&A, 477, 193
Mehner, A., de Wit, W. J., Groh, J. H., et al. 2016, A&A, 585, A81
Molinari, S., Swinyard, B., Bally, J., et al. 2010, A&A, 518, L100
Muratore, M. F., Kraus, M., Oksala, M. E., et al. 2015, AJ, 149, 13
Oksala, M. E., Kraus, M., Cidale, L. S., et al. 2013, A&A, 558, A17
Oudmaijer, R. D., & Drew, J. E. 1999, MNRAS, 305, 166
Poglitsch, A., Waelkens, C., Geis, N., et al. 2010, A&A, 518, L2
Rohlfs, K., & Wilson, T. L. 2004, Tools of Radio Astronomy (Berlin: Springer)
Šlechta, M., & Škoda, P. 2002, PAICz, 90, 1
Smith, L. J., Norris, R. P. F., & Crowther, P. A. 2002, MNRAS, 337, 1309
Smith, N., Bally, J., & Walawender, J. 2007, AJ, 134, 846
The, P. S., de Winter, D., & Perez, M. R. 1994, A&AS, 104, 315
Vassilev, V., Meledin, D., Lapkin, I., et al. 2008, A&A, 490, 1157
Watson, C., Povich, M. S., Churchwell, E. B., et al. 2008, ApJ, 681, 1341
Werner, M. W., Roellig, T. L., Low, F. J., et al. 2004, ApJS, 154, 1
Wheelwright, H. E., de Wit, W. J., Weigelt, G., et al. 2012, A&A, 543, A77
Wilson, T. L., & Rood, R. 1994, ARA&A, 32, 191
Wright, E. L., Eisenhardt, P. R. M., Mainzer, A. K., et al. 2010, AJ, 140, 1868
Yamaguchi, R., Akira, M., & Yasuo, F. 1999, in Star Formation 1999, ed. T. Nakamoto (Nobeyama: Nobeyama Radio Observatory), 383
Zickgraf, F.-J. 2003, A&A, 408, 257